

Spurious forces can dominate the vorticity budget of ocean gyres on the C-grid

Andrew Styles^{1,1}, Michael Bell^{2,2}, David Marshall^{1,1}, and David Storkey^{2,2}

¹University of Oxford

²Met Office

November 30, 2022

Abstract

Gyres are prominent surface structures in the global ocean circulation that often interact with the sea floor in a complex manner. Diagnostic methods, such as the depth-integrated vorticity budget, are needed to assess exactly how such model circulations interact with the bathymetry. Terms in the vorticity budget can be integrated over the area enclosed by streamlines to identify forces that spin gyres up and down. In this article we diagnose the depth-integrated vorticity budgets of both idealized gyres and the Weddell Gyre in a realistic global model. It is shown that spurious forces play a significant role in the dynamics of all gyres presented and that they are a direct consequence of the Arakawa C-grid discretization and the z-coordinate representation of the sea floor. The spurious forces include a numerical beta effect and interactions with the sea floor which originate from the discrete Coriolis force when calculated with the following schemes: the energy conserving scheme (ENE); the enstrophy conserving scheme (ENS); and the energy and enstrophy conserving scheme (EEN). Previous studies have shown that bottom pressure torques provide the main interaction between the depth-integrated flow and the sea floor. Bottom pressure torques are significant, but spurious interactions with bottom topography are similar in size. Possible methods for reducing the identified spurious topographic forces are discussed. Spurious topographic forces can be alleviated by using either a B-grid in the horizontal plane or a terrain-following vertical coordinate.

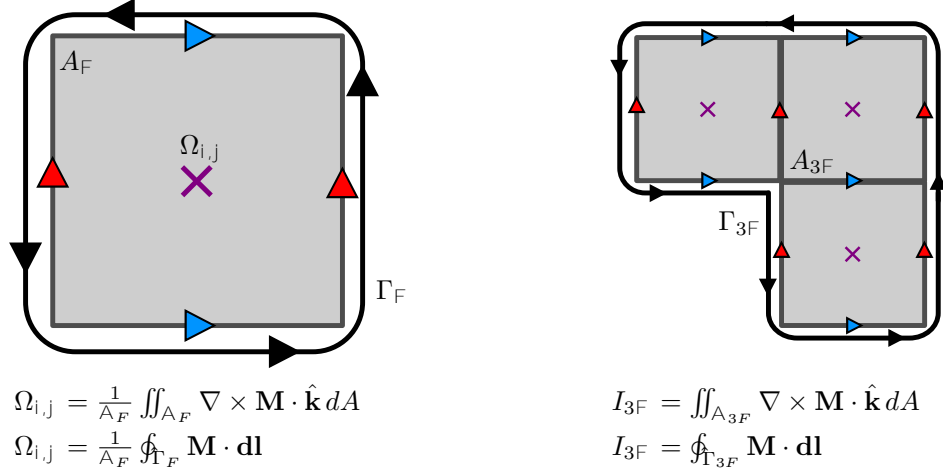


Figure 3. The application of Stokes' theorem on a C-grid. The vorticity diagnostic Ω is equivalent to the normalized line integral of \mathbf{M} around a single F cell of area A_F . The area integral of Ω over a collection of F cells (e.g. A_{3F}) is equivalent to the line integral of \mathbf{M} along the perimeter (e.g. Γ_{3F}).

the contour, the local domains for calculating the grid point divergences will overlap meaning the resultant area integral will not satisfy the divergence theorem in general.

4 A double gyre model

4.1 Details of the configuration

The first experiment in this article is an idealized double gyre configuration based on the GYRE PISCES reference configuration in NEMO. The GYRE PISCES reference configuration has been used for a wide range of experiments (Lévy et al., 2010, 2015; Ruggiero et al., 2015; Perezhogin, 2019). The domain is a closed rectangular basin which is 3180 km long, 2120 km wide, and is rotated at an angle of 45° relative to the zonal direction. The basin exists on a beta plane where f varies linearly around its value at 30°N .

The model has a regular 122×82 grid that is aligned with the rotated basin. The horizontal resolution is equivalent to a $1/4^\circ$ grid at the equator and the configuration has 31 model levels. Two forms of bathymetry are used in this section. The FLAT configuration has a fixed depth of 4.5km and no partial cells are used. The SLOPED configuration has a linear slope that extends from the North West side of the basin and spans half the basin (see Figure 4a). The maximum depth of the SLOPED configuration is 4.5km, the minimum depth is 2km, and partial cells are used to represent the slope.

The circulation is forced by sinusoidal analytic profiles of surface wind stress and buoyancy forcing. The wind stress is zonal and only varies with latitude so that the curl changes sign at 22°N and 36°N (see Figure 4b). The wind stress profile is designed to spin up a subpolar gyre in the north, a subtropical gyre in the south, and a small recirculation also emerges in the bottom corner. The net surface heat flux takes the form of a restoring to a prescribed apparent temperature. Further details about the buoyancy forcing can be found in Lévy et al. (2010). The wind stress and buoyancy forcing varies seasonally in a sinusoidal manner.

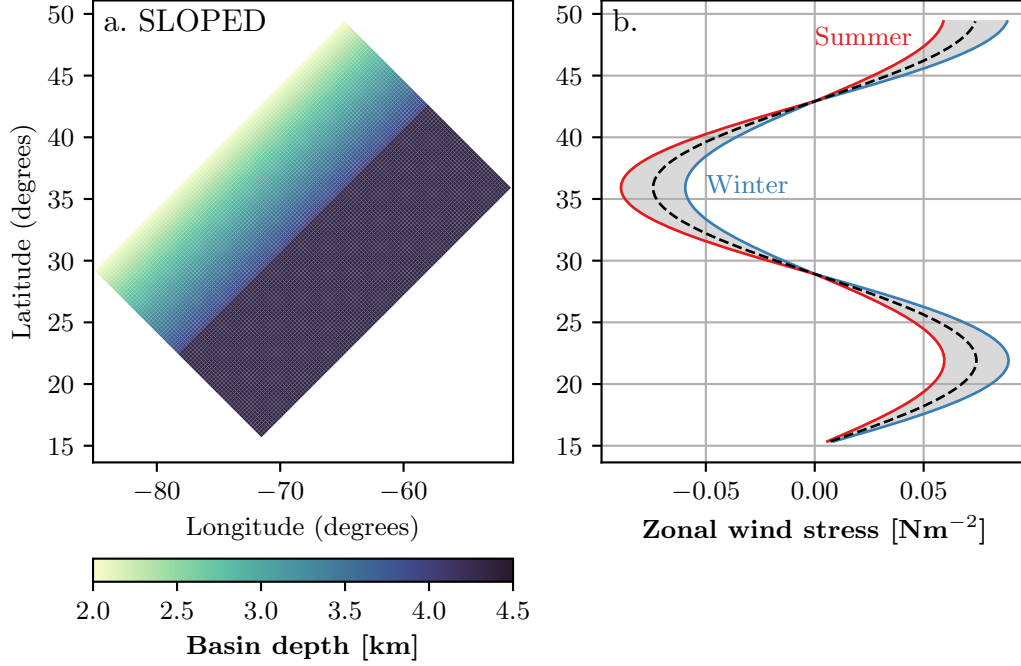


Figure 4. (a) Bathymetry of the SLOPED configuration. (b) The wind stress profile for both the FLAT and SLOPED configuration. The wind stress profile varies seasonally in a sinusoidal manner between summer and winter extremes that are highlighted.

The model uses a free slip condition on all boundaries except at the bottom where a linear friction drag is applied. A simplified linear equation of state is used with a thermal expansion coefficient of $\alpha_0 = 2 \cdot 10^{-4} \text{kg m}^{-3} \text{K}^{-1}$, and a haline coefficient of $\beta_0 = 7.7 \cdot 10^{-4} \text{kg m}^{-3} \text{psu}^{-1}$. Horizontal and biharmonic diffusion of momentum is implemented with a diffusivity of $5 \cdot 10^{10} \text{m}^4 \text{s}^{-1}$. Biharmonic diffusion of tracers along isopycnals is implemented with a diffusivity of $10^9 \text{m}^4 \text{s}^{-1}$.

The model is spun up for 60 years and the experiment was run for an additional 10 years with monthly-mean outputs. A steady state is not required for the diagnostics to be valid as the time derivative term is present in the vorticity budget. A time step of 10 minutes is used for the model integration.

The EEN vorticity scheme is used for consistency with all analysis discussed in Section 3 and the results from the Weddell Gyre in Section 5. The EEN method calculates F cell thicknesses using the method described by Equation 13 and we therefore expect sudden changes in the F cell thickness near the domain edge for both the FLAT and SLOPED configurations.

4.2 Methods

Momentum diagnostics are calculated for every time step and the discrete vorticity diagnostics are calculated by depth-integrating the momentum diagnostics and taking the curl. The resultant diagnostics are time-averaged over the ten year experimental period. The extensive time-averaging will influence the advection vorticity diagnostic as there is an added contribution from the eddy vorticity flux.

For contour integration, the vorticity diagnostics and depth-integrated stream function are then linearly interpolated onto a regular $1/12^\circ$ grid. This is to minimise errors caused by the difference between the true enclosed streamline area and the total area of the enclosed F cells. Interpolation beyond $1/12^\circ$ resolution makes little difference to the results, suggesting that the area error has been significantly suppressed.

For 1001 values of ψ , closed streamline contours are identified using a marching squares algorithm from the scikit-image package (Van Der Walt et al., 2014). Streamlines that are near the recirculation gyre (south of 20°N) are ignored in this experiment and for some values of ψ no closed streamlines could be found. For each closed streamline found, the vorticity diagnostics are integrated over the area enclosed; this is equivalent to calculating $I(\psi)$ in Equation 4 over many values of ψ . The freshwater fluxes mean that $\mathbf{r}_h \cdot \mathbf{U} \neq 0$ even in a steady state and an exact stream function cannot be calculated. To test how closely the calculated streamlines follow the circulation we integrate the positive quantity $\int f_0 (\mathbf{r}_h \cdot \mathbf{U}) \cdot \mathbf{j}$ over the same enclosed areas to estimate the magnitude of the error caused by the divergent flow. The maximum value of f is used as f_0 and the largest contour integral of $\int f_0 (\mathbf{r}_h \cdot \mathbf{U}) \cdot \mathbf{j}$ is 0.16 Sv/day which is substantially smaller than the leading contour integrals presented in the next sub-section. In addition to this test we used an elliptical solver to decompose the depth-integrated flow into compressible and incompressible parts; using the streamlines from the incompressible component does not change the results presented in the next sub-section.

Multiple closed contours can be found for the same value of ψ so an additional contour constraint is needed to ensure $I(\psi)$ is single-valued. In this experiment we always choose the contour that spans the largest area which minimises the influence of small pocket circulations that are not a part of the gyre. Closed streamlines that run along the edge of the domain can be hard to identify so a discontinuity in $I(\psi)$ near $\psi = 0$ is expected as the largest detected contours will suddenly become pocket circulations as ψ approaches zero.

4.3 Results

The depth-integrated streamfunction from the FLAT and SLOPED configurations is shown in Figure 5. The vorticity of the depth-integrated velocity field is shown in Figure 6. In both configurations a subtropical and subpolar gyre can clearly be identified and a small recirculation gyre can be found in the Southernmost corner. The subtropical gyre circulation is clockwise and the subpolar gyre circulation is anticlockwise.

In the FLAT configuration the subtropical gyre has a transport of 65 Sv and the subpolar gyre has a transport of 18 Sv. In the SLOPED configuration the subtropical gyre has a transport of 38 Sv and the subpolar gyre has a transport of 14 Sv. We note that the sloped bathymetry significantly alters the form of the subtropical gyre streamlines.

The depth-integrated vorticity diagnostics of the FLAT and SLOPED configurations are shown in Figures 7 and 8 respectively alongside the decomposition of the planetary vorticity diagnostic introduced in Section 3.4. In the FLAT configuration we note that the non-linear advection of vorticity and the planetary vorticity diagnostic have the largest grid point values ($\sim 10^{-9} \text{ m s}^{-2}$) near the western boundary currents of both gyres. The wind stress curl is one order of magnitude smaller ($\sim 10^{-10} \text{ m s}^{-2}$) but changes sign less frequently within the gyre regions. We see that the planetary vorticity diagnostic is almost entirely a result of the beta effect (Figure 7g and h). We note that the contribution from varying cell thicknesses in the FLAT configuration is non-zero and localized to the edge (Figure 7j) where the EEN Coriolis scheme artificially shrinks F cell thicknesses near masked points.

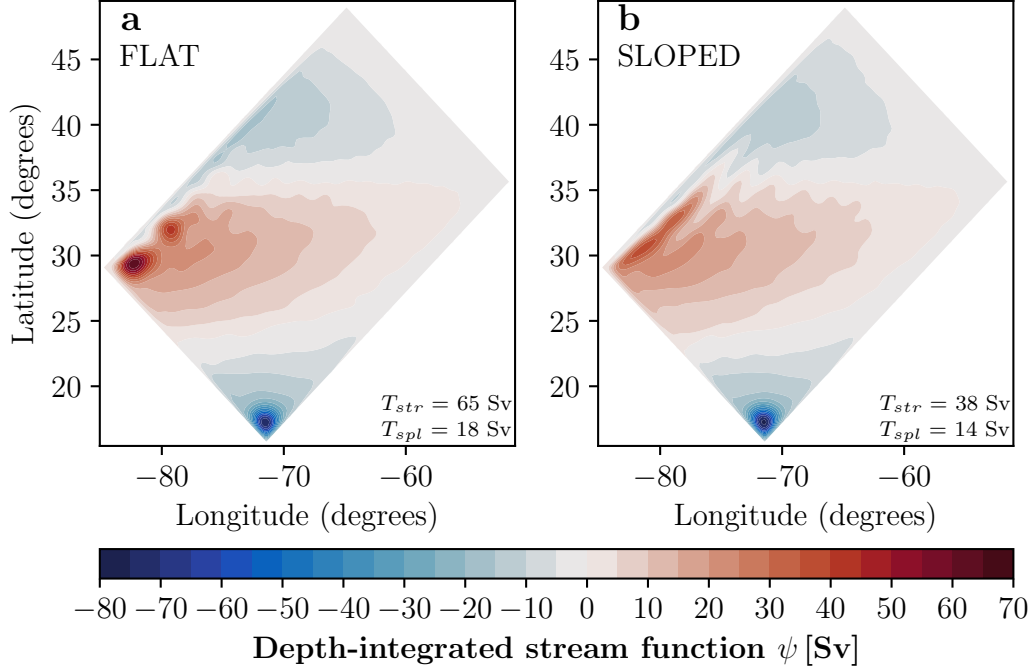


Figure 5. The depth-integrated streamfunction (time-averaged) of the (a) FLAT and (b) SLOPED configurations. The transports of the subtropical gyre (T_{str}) and subpolar gyre (T_{spl}) are given.

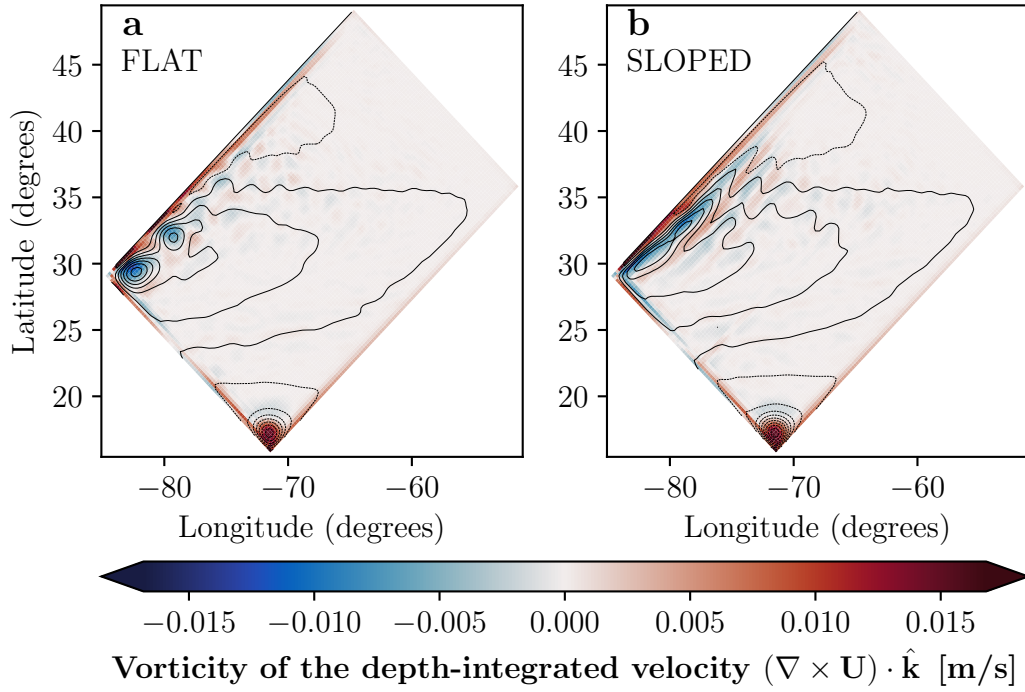


Figure 6. The vorticity of the depth-integrated velocity field (time-averaged) for the (a) FLAT and (b) SLOPED configurations. The black contours are streamlines from Figure 5.

Figure 7. The depth-integrated vorticity diagnostics for the FLAT configuration and the components of the planetary vorticity diagnostic (time-averaged). Panels (a) through to (g) are the diagnostics for the terms in the depth-integrated vorticity equation (Equation 2). Panels (h) through to (l) are the components of the planetary vorticity diagnostic in Equation 23 and discussed in Section 3.4. The color bar is logarithmic (for values greater than 10^{-11} in magnitude) and shows the four leading order magnitudes that are positive and negative.

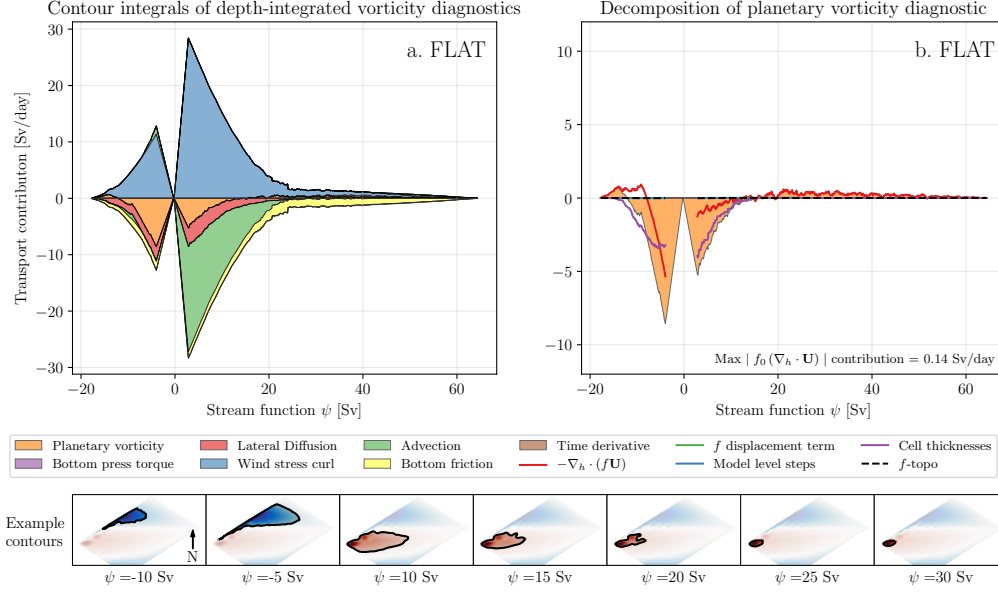


Figure 9. Stacked area plots showing the integrals of depth-integrated vorticity diagnostics (time-averaged) for the FLAT configuration. Positive values correspond to a force that spins the subtropical (> 0) or subpolar (< 0) gyre up. The diagnostics are integrated over areas enclosed by streamlines to develop a full forcing profile of the gyres. The x axis describes the value of the streamline used in the integration. Example streamline contours are given. (b) Shows the area integrals of the planetary vorticity diagnostic and its components. The maximum contour integral of $|f_0(\nabla_h \cdot \mathbf{U})|$ is stated as an approximate error caused by the divergence of the depth-integrated flow.

In the SLOPED configuration (Figure 8) the advection and planetary vorticity diagnostics are still large but have an elongated structure similar to the SLOPED streamlines in Figure 5b. The bottom pressure torque is significant and is localized to the sloped region (Figure 8b). The planetary vorticity diagnostic has a more complex decomposition as the influence of varying cell thicknesses extends beyond the edge of the domain and model level steps also contribute (Figure 8k).

The integrals of the vorticity diagnostics over areas enclosed by streamlines are shown in Figure 9 and Figure 10 for the FLAT and SLOPED configurations respectively as well as the integrals of the planetary vorticity diagnostic components. The integrals are given in units of Sv/day to describe the tendency for model forces to increase or decrease the gyre transport over time. Example streamline contours are also shown. In these figures $\psi > 0$ describes the subtropical gyre and $\psi < 0$ describes the subpolar gyre. The subtropical and subpolar gyres circulate in the opposite direction but the sign of the integration results are adjusted so that positive integrals correspond to forces that spin the gyres up.

In the FLAT configuration we see that the subtropical and subpolar gyre are entirely driven by wind stress curl. At the exterior of the subtropical gyre (small and positive values of ψ) the wind stress curl is largely balanced by the advection of relative vorticity which implies a net import of positive vorticity into the gyre. The imported vorticity cannot originate from the subpolar gyre as the advection of relative vorticity plays no role in spinning the subpolar gyre down. The streamlines at the exterior of the gyre

Figure 10. Stacked area plots showing the integrals of depth-integrated vorticity diagnostics (time-averaged) for the SLOPED configuration. Positive values correspond to a force that spins the subtropical (> 0) or subpolar (< 0) gyre up. (b) Shows the area integrals of the planetary vorticity diagnostic and its components.

envelop both cells (maxima in β) of the subtropical gyre so the advection of vorticity between the cells is not a contribution to the signal. The imported vorticity must originate from the recirculation gyre in the southernmost corner. In the subtropical gyre interior the wind stress curl is largely balanced by the curl of bottom friction, matching the balance proposed by Niiler (1966).

The planetary vorticity diagnostic is significant in both of the FLAT gyres and is the dominant drag for the subpolar gyre. At both gyre exteriors (small values of β) the integrated planetary vorticity diagnostic is a combination of a numerical beta effect originating from the discrete calculation of $r_h(fU)$ and the influence of partial F cells that are artificially created by the EEN scheme. At the interior of both gyres (large values of β) the numerical beta effect is the only component.

In the SLOPED configuration we see that both the subtropical and subpolar gyre are almost entirely driven by wind stress curl. There is no dominant force spinning the gyres down. Advection, bottom pressure torques, lateral diffusion, bottom friction, and planetary vorticity all make a similar contribution to spinning the gyres down. The planetary vorticity diagnostic is similarly mixed as both the numerical beta effect and partial cells make up the signal. The gyres in the SLOPED configuration appear to be an intermediate case between a topographically steered gyre and an advective regime.

Spurious forces that emerge from the discrete Coriolis acceleration are significant in idealised models with and without variable bathymetry and appear to have a large influence on gyre circulations. In the next sub-section we see if these forces are also significant in a realistic global model.

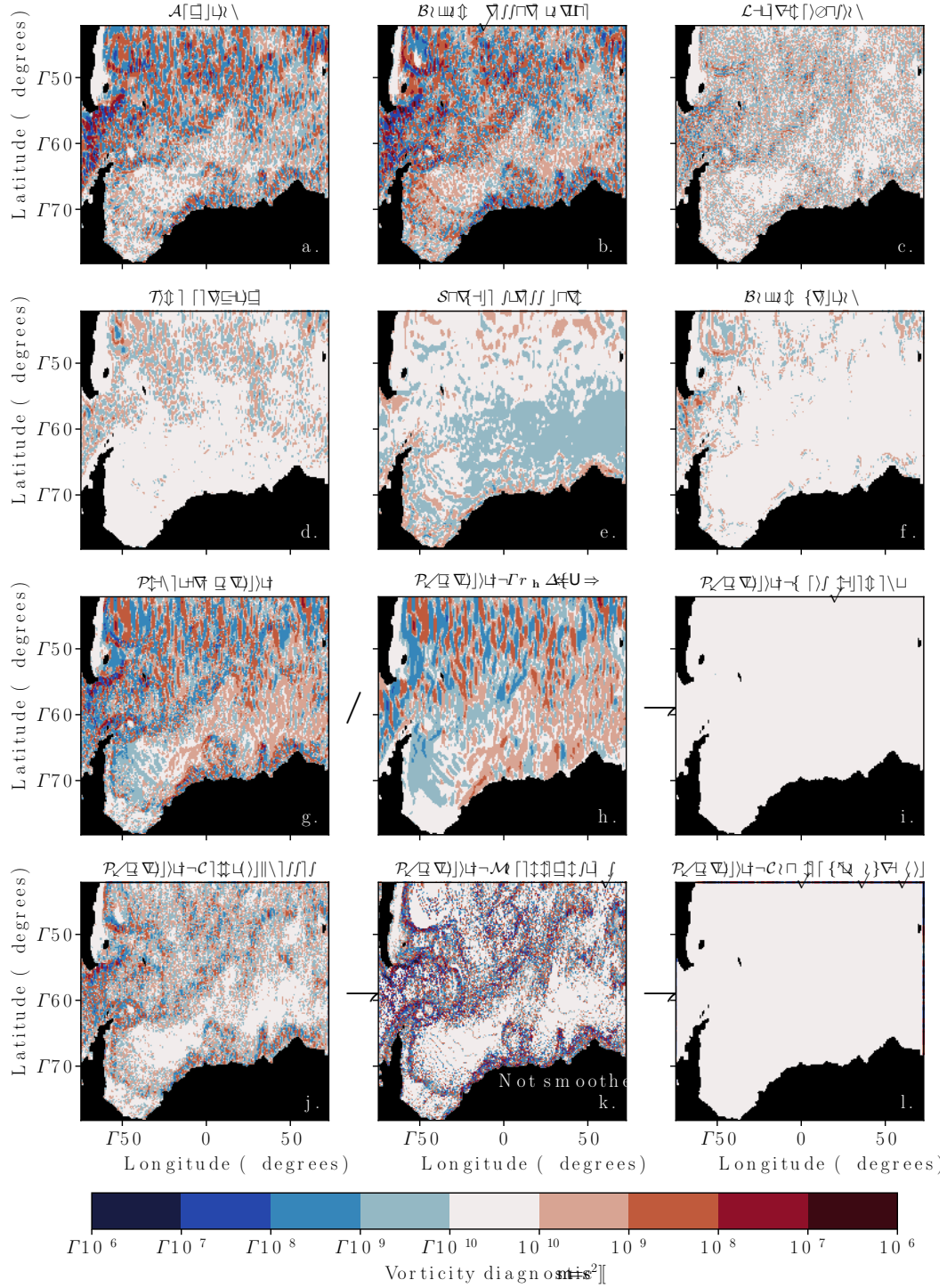


Figure 13. The depth-integrated vorticity diagnostics for the Weddell Gyre and the components of the planetary vorticity diagnostic (time-averaged). All fields except (k) have gone through a 25 point nearest neighbour smoothing process.

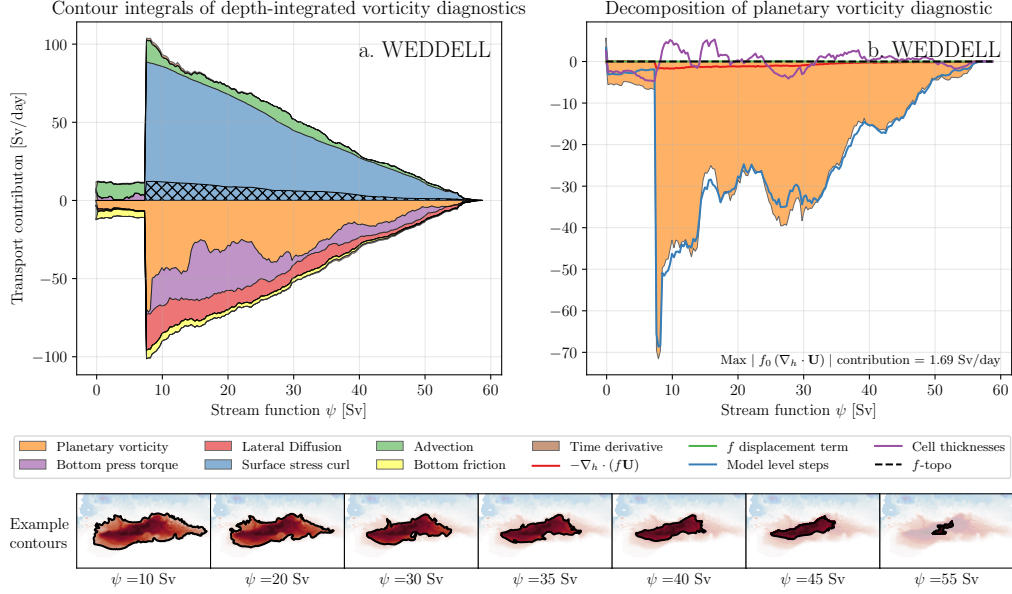


Figure 14. Stacked area plots showing the integrals of depth-integrated vorticity diagnostics for the Weddell Gyre (time-averaged). Positive values correspond to a force that spins the gyre up. The hatching marks the sea ice contribution to the surface stress integral. (b) Shows the area integrals of the planetary vorticity diagnostic and its components.

analysis in Section 3.2 is general for three popular schemes: EEN, ENE, and ENS. The methods and decomposition used in this article are applicable under any scheme where the Coriolis acceleration can be expressed in the form of Equations 8 and 9. Results from the SLOPED double gyre configuration using the different schemes are presented in Appendix C and the vorticity budgets are qualitatively similar. Spurious topographic forces and the numerical beta effect are still significant.

It therefore seems that switching between the available vorticity schemes will not alleviate the spurious signal. It is possible that a new scheme could be formulated which is designed to significantly reduce the spurious forces, but that will most likely require abandoning the conserved quantities that characterise the existing schemes.

6.2 Alternative depth-integrated vorticity equations

In Section 2.1 we derived a depth-integrated vorticity equation by taking the curl of the depth-integrated momentum equation and we calculated the model vorticity diagnostics using the equivalent discrete method. As discussed in Section 2.1, there are alternative formulations of the depth-integrated vorticity equations with different physical meanings. An accurate model should be able to represent all forms of the depth-integrated vorticity budget so switching between formulations does not alleviate any spurious forces, but it is interesting to see if any of the spurious contributions in this article can spill over into other vorticity budgets.

If we derive a continuous depth-integrated vorticity equation by depth-integrating the curl of the momentum equations then the Coriolis acceleration emerges in the vor-

676 ticity budget as:

$$\frac{\partial}{\partial t} \int_{H(x,y)} \mathbf{r} \cdot \hat{\mathbf{k}} dz = \int_{H(x,y)} \mathbf{r} \cdot \nabla_h (f\mathbf{U}) + f(\mathbf{u}_b \cdot \mathbf{r}) H + f(\mathbf{u}_t \cdot \mathbf{r}) \eta, \quad (24)$$

677 where \mathbf{u}_t and \mathbf{u}_b are the horizontal velocities at the free surface and sea floor respectively.
 678 When compared with Equation 2 we can see that the planetary vorticity term has an
 679 additional topographic and free surface term. The second term on the right hand side
 680 of Equation 24 describes a vortex stretching acting on the vertical velocity induced by
 681 the bottom topography. In configurations with no variable bathymetry and small vari-
 682 ations in the free surface, the order of taking the curl and depth-integrating no longer
 683 affects the vorticity budget so the non-topographic spurious forces identified in this ar-
 684 ticle will remain in either formulation.

685 To calculate the discrete curl of a horizontal vector field near the bathymetry we
 686 need to make an assumption about how the along-slope component varies as it approaches
 687 the edge of the domain. We can assume either a free slip or no slip boundary condition
 688 by using a ghost point that mirrors the location of the closest grid point into the bathymetry.
 689 For a free slip boundary condition the ghost point value matches the closest grid point
 690 value, F^k ; for a no slip boundary condition the ghost point value will be the negative
 691 of the closest grid point value, $-F^k$. A partial slip boundary condition also exists where
 692 the value of the ghost point will be between $-F^k$ and F^k .

693 Let us return to the simple flow introduced in Section 3.3 and illustrated in Fig-
 694 ure 2 but this time when we calculate the planetary vorticity diagnostic we will calcu-
 695 late the curl of the Coriolis acceleration on each model level and then depth-integrate.
 696 For the lower level, the horizontal flow is entirely in the x direction so there is a zero along-
 697 slope component of the Coriolis acceleration near the bathymetry ($F^k=0$). This means
 698 that if a free slip, no-slip, or partial slip boundary condition are used the ghost point value
 699 will be zero and the curl of the Coriolis force (centred on the purple cross in Figure 2)
 700 will be zero in all three cases. As all vorticity generation takes place in the upper level,
 701 the planetary vorticity diagnostic is the same if we take the curl before or after depth-
 702 integrating (Equation 21) and the effect of model level steps can exist in either vortic-
 703 ity budget.

704 The result of Equation 21 can be interpreted as a vortex stretching acting on the
 705 vertical velocity U_1 . The vertical velocity seems unlikely to originate from topographic
 706 upwelling as there is no flow in the y direction. This fact combined with the ambiguity
 707 of $\mathbf{r} \cdot \nabla H$ at model level steps means we would advise caution before comparing the dis-
 708 crete vortex stretching that originates from model level steps to the analytic vortex stretch-
 709 ing in Equation 24.

710 6.3 The B-grid

711 Altering the grid geometry can significantly change the behaviour of model forces.
 712 To highlight this we consider how the Coriolis force behaves on the B-grid. The B-grid
 713 excels at representing geostrophic flows as u , and v are located on the same vector point.
 714 The streamfunction and relative vorticity are located on the tracer point as shown in Fig-
 715 ure 15.

716 On the B-grid the Coriolis acceleration is simply:

$$\text{COR}_{ij,k}^x = f_{ij} v_{ij,k}, \quad (25)$$

$$\text{COR}_{ij,k}^y = f_{ij} u_{ij,k}. \quad (26)$$

717 The Coriolis acceleration does not rely on multi-point averaging or thickness weighting
 718 of f so numerical contributions do not emerge in the grid point acceleration.

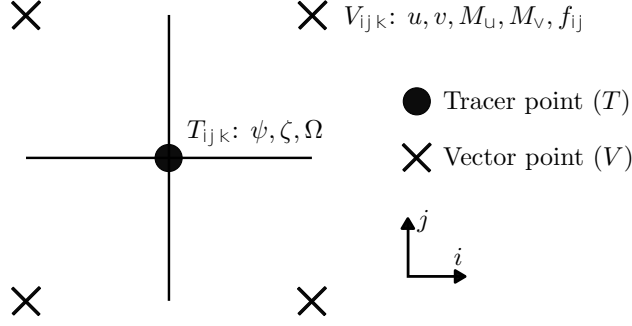


Figure 15. The horizontal distribution of variables on the B-grid. Tracer points (T) and vector points (V) are shown alongside important values that are centred on these points. Just like in the C-grid, the vertical velocities are found directly above and below the Tracer point.

On the B-grid u and v lie on the same point so they share the same mask. This means that non-zero Coriolis accelerations are never masked near model level steps and the depth-integrated Coriolis acceleration is a function of the depth-integrated velocities only:

$$\widehat{\text{COR}}_{ij}^x = f_{ij} V_{ij}, \quad (27)$$

$$\widehat{\text{COR}}_{ij}^y = f_{ij} U_{ij}, \quad (28)$$

We therefore conclude that the spurious force caused by model level steps on the C-grid (see Section 3.3) is not present on the B-grid. The corresponding planetary vorticity diagnostic is equal to $\mathbf{r} \cdot \nabla \times (f\mathbf{U})$ calculated over a single tracer cell.

Calculating the curl on a B-grid is consistent with Stokes' law applied to a tracer cell but the vector information is found on the corners of the cell. As the stream function is defined on the tracer point we can approximate that the area enclosed by a streamline is a collection of interior tracer cells. Similarly to the C-grid case in Section 3.5 this is an approximation as we are assuming that the streamline follows the rectangular edges of the interior tracer cells so interpolation may be required to remove any significant area error. Unlike the C-grid case, the planetary vorticity diagnostic is equal to $\mathbf{r} \cdot \nabla \times (f\mathbf{U})$ calculated over a single tracer cell. Therefore, the area integral of the planetary vorticity diagnostic will satisfy the divergence theorem applied to the internal tracer cells. It seems likely that this discrete integral may vanish on a sufficiently fine grid but further investigation with idealized and realistic streamlines is needed.

Using the B-grid would remove all of the spurious topographic forces identified in this article. This highlights how a model circulation's interaction with the sea floor is significantly affected by the grid geometry.

6.4 Terrain-following coordinates

The spurious topographic effects found in this article are a consequence of how bottom topography is represented in z -coordinates. In the Weddell Gyre especially we see how model level steps can create large spurious contributions to the depth-integrated vorticity budget.

Terrain-following coordinates (or σ -coordinates) are an alternative form of vertical coordinate where the vertical resolution adjusts with the bottom topography so that the same number of model levels are present in all fluid columns (Song & Haidvogel, 1994). σ -coordinates are used in Stewart et al. (2021), Schoonover et al. (2016), and Jackson

et al. (2006) and have the advantage of removing spurious terms that emerge from model level steps. The forms of the EEN, ENE, and ENS vorticity schemes are unchanged when using terrain-following coordinates so the horizontal variations in cell thicknesses could still cause a spurious signal.

Terrain-following coordinates are not used widely in climate models because of the difficulty in calculating accurate horizontal pressure gradients (near the equator), advection, and isoneutral tracer advection. A full discussion of the current advantages and limitations of terrain following coordinates can be found in Lemarié et al. (2012).

6.5 Isopycnal coordinates and the vertical Lagrangian-remap method

In isopycnal C-grid models, where density is used as a vertical coordinate, cell thicknesses still vary and in models with many density layers the model levels are free to incrop to the sea floor. The forms of the EEN, ENS, and ENE schemes are unchanged when using density coordinates so the spurious signals in the planetary vorticity diagnostic seem to be possible. In configurations where density layers infrequently incrop to the sea floor, the effect of model level steps will be significantly suppressed as the grid is approaching the limit of a terrain-following coordinate system.

In C-grid models that use the vertical Lagrangian-remap method (Bleck, 2002; Adcroft et al., 2019) the vertical coordinate evolves with the flow and is then conservatively remapped onto a target grid (see Griffies et al. (2020) for a review). The forms of the EEN, ENS, and ENE schemes are unchanged when using this method. If the target coordinate grid still has horizontal variations in cell thicknesses and incrops with the sea floor, we would expect there to be spurious topographic interactions with the sea floor. It is possible that in areas of topographic upwelling the effect of model level steps could be reduced as Coriolis accelerations near the bathymetry are elevated by the vertical motion and are partially projected onto unmasked points when remapped onto the target grid.

7 Summary

The depth-integrated vorticity budget is a valuable tool for identifying important model forces in gyre circulations. Vorticity diagnostics can be integrated over the area enclosed by streamlines to identify forces responsible for spinning the gyre up and down. By considering how the vorticity budget is represented on a C-grid with step-like bathymetry we identified spurious forces that emerge from the representation of bottom topography and the discrete Coriolis acceleration. Model level steps and partial cells produce two distinct spurious topographic forces. In the absence of bottom topography, it is shown that the discrete planetary vorticity term does not generally vanish when integrated over the discrete area enclosed by a streamline. This suggests that a spurious non-topographic force, described as a numerical beta effect, is also present.

We first studied the vorticity budget of an idealized double gyre configuration with analytic geometry, forcing, and two bathymetry options. The FLAT variant has a constant depth and the SLOPED variant has a linear slope that extends over half the domain. The subtropical gyre of the FLAT configuration is non-linear at the exterior (wind stress curl balanced by advection) and is in a Stommel (1948) regime in the interior (wind stress curl balanced by friction). The FLAT subpolar gyre is spun up by wind stress curl and mostly spun down by spurious forces found in the planetary vorticity diagnostic. Spurious forces are significant in both FLAT gyres and are a consequence of the numerical beta effect and partial F cells that are artificially introduced by the EEN vorticity scheme. Artificial partial F cells would not be present in the ENS or ENE vorticity schemes.

The vorticity budget of the SLOPED gyres features bottom pressure torques and an increased influence of partial cells on the planetary vorticity diagnostic. The SLOPED subtropical gyre is an intermediate case between a topographically steered gyre and a non-linear circulation. The SLOPED subpolar gyre is driven by wind stress curl but spun down by the combined effect of bottom pressure torques and spurious interactions with the topography via partial cells. This first case study highlighted how spurious terms can dominate a vorticity budget in idealized configurations with and without variable bathymetry.

The second case study was the Weddell Gyre in a global model where the forcing and geometry are more realistic. By studying the vorticity budget of the Weddell Gyre we conclude that the model circulation is mostly spun up by wind stress curl and spun down by the combined effect of bottom pressure torques and spurious interactions with the topography. The largest of the topographic forces spinning the Weddell Gyre down is the spurious and unrealistic force caused by model level steps.

Switching to alternative vorticity schemes is not effective at reducing spurious contributions to the vorticity budget. By presenting a general form of the discrete Coriolis acceleration we are able to quickly conclude that the topographic and non-topographic spurious forces will remain under all three vorticity schemes and any other scheme that uses this general form. The influence of model level steps is a direct consequence of the C-grid geometry when using vertical coordinates that intersect the bathymetry and is relatively insensitive to the choice of vorticity scheme.

Altering the geometry of the discretisation is an effective method for reducing spurious topographic forces. The B-grid is better at representing the Coriolis force and it is not possible for model level steps or partial cells to influence the Coriolis acceleration. Model level steps and their influence on the Coriolis acceleration can be avoided altogether by using terrain-following coordinates.

The B-grid and terrain-following coordinates have their own unique limitations and it is unclear how much the identified spurious forces corrupt circulation variables such as the gyre transport. It is possible that the spurious forces are inadvertently performing the role of one or more real ocean processes that are required for accurate simulations. If a combination of non-spurious forces can fully account for the spurious forces found in this article then the identified problem is purely diagnostic in nature. Otherwise, any part of the spurious forcing that cannot be accounted for by non-spurious forces should be considered as a numerical error. This numerical error could be small but may also accumulate under specific conditions and corrupt model circulations. The spurious cooling (Hecht, 2010) that occurs when a dispersive advection scheme is used with the Gent and McWilliams (1990) eddy parametrization highlights the dangers of ignoring numerical errors.

It is also possible that other model forces contain spurious contributions that have not been uncovered in this article. These contributions could be significant and may have the potential to cancel the spurious effects found in this article. When looking at the integrated diagnostics in Figures 9, 10, and 14 we see that usually the only model force with an opposite contribution to the Coriolis force that is large enough to cancel the found spurious effects is the surface stress. It seems unlikely that the surface stress contains spurious contributions that are closely tied to bathymetry and the Coriolis parameter.

It is important for the ocean modelling community to continue developing new ways of representing bathymetry and we hope that vorticity budgets and the diagnostic method presented in this article will provide a valuable tool for assessing and quantifying representations of the sea floor in current and future ocean models.

Appendix A Deriving the depth-integrated vorticity equation

Here we derive the depth-integrated vorticity equation (Equation 2) including the omitted contributions from surface undulations and atmospheric pressure torques. We start from the vector invariant form of the momentum equation,

$$\frac{\partial \mathbf{u}_h}{\partial t} = (\mathbf{r} \cdot \nabla) \mathbf{u} + \frac{1}{2} \mathbf{r} \times (\nabla \times \mathbf{u}) - f \hat{\mathbf{k}} \times \mathbf{u} - \frac{1}{\rho_0} \mathbf{r} \times \nabla P + \mathbf{F}^u + \mathbf{D}^u, \quad (\text{A1})$$

which has already been introduced in Section 2.1. To derive the depth-integrated vorticity equation, we must first depth-integrate the equation and then calculate the vertical component of the curl. In this appendix, we consider how each term in Equation A1 is transformed by this operation.

When depth-integrating the time derivative term in Equation A1, we must respect the time dependency of the free surface, η . We therefore use the Leibniz integration rule,

$$\mathbf{r} \int_{H(x,y)}^{(\eta(x,y),t)} \frac{\partial \mathbf{u}_h}{\partial t} dz - \hat{\mathbf{k}} = \frac{\partial}{\partial t} (\mathbf{r} \times \mathbf{U}) \cdot \hat{\mathbf{k}} - \mathbf{r} \times \mathbf{u}_h(z=\eta) \frac{\partial \eta}{\partial t} \cdot \hat{\mathbf{k}}, \quad (\text{A2})$$

where the second term on the right hand side of Equation A2 is the contribution from free surface undulations.

The non-linear term in Equation A1 can be rewritten as,

$$(\mathbf{r} \cdot \nabla) \mathbf{u} + \frac{1}{2} \mathbf{r} \times (\nabla \times \mathbf{u}) = \frac{1}{2} \mathbf{r} \times (\mathbf{u}_h \times \nabla_h) + \zeta \hat{\mathbf{k}} \times \mathbf{u}_h + w \frac{\partial \mathbf{u}_h}{\partial z}. \quad (\text{A3})$$

The non-linear term emerges as the advection term in the depth-integrated vorticity equation and we note that,

$$\mathbf{r} \int_H \zeta \hat{\mathbf{k}} \times \mathbf{u}_h dz - \hat{\mathbf{k}} = \mathbf{r} \times \int_H \zeta \mathbf{u}_h dz. \quad (\text{A4})$$

Similarly the curl of the depth-integrated Coriolis acceleration is the planetary vorticity term,

$$\mathbf{r} \int_H f \hat{\mathbf{k}} \times \mathbf{u}_h dz - \hat{\mathbf{k}} = \mathbf{r} \times \int_H (f \mathbf{U}). \quad (\text{A5})$$

When depth-integrating the pressure gradient in Equation A1, we must respect the x and y dependency of the sea floor and the free surface. We therefore use the Leibniz integration rule,

$$\mathbf{r} \int_{H(x,y)}^{(\eta(x,y),t)} \frac{1}{\rho_0} \mathbf{r} \times \nabla P dz - \hat{\mathbf{k}} = \frac{1}{\rho_0} (\mathbf{r} \times P_b - \mathbf{r} \times H) \cdot \hat{\mathbf{k}} + \frac{1}{\rho_0} (\mathbf{r} \times P_a - \mathbf{r} \times \eta) \cdot \hat{\mathbf{k}}, \quad (\text{A6})$$

where P_a is the atmospheric pressure at the free surface. The second term on the right hand side of Equation A6 is the atmospheric pressure torque.

The surface forcing term in Equation A1 emerges as the difference between the curl of the top and bottom stresses,

$$\mathbf{r} \int_H \mathbf{F}^u dz - \hat{\mathbf{k}} = \frac{1}{\rho_0} (\mathbf{r} \times \tau_{\text{top}}) \cdot \hat{\mathbf{k}} - \frac{1}{\rho_0} (\mathbf{r} \times \tau_{\text{bot}}) \cdot \hat{\mathbf{k}}, \quad (\text{A7})$$

$$(\text{A8})$$

and the diffusion term emerges as \mathbf{D} ,

$$\mathbf{r} \int_H \mathbf{D}^u dz - \hat{\mathbf{k}} = \mathbf{D}. \quad (\text{A9})$$

By combining all the equations above we can derive the depth-integrated vorticity equation,

$$\begin{aligned} \frac{\partial}{\partial t} (\mathbf{r} \cdot \mathbf{U}) \cdot \hat{\mathbf{k}} = & \mathbf{r} \cdot \mathbf{h} (f\mathbf{U}) + \frac{1}{\rho_0} (\mathbf{r} \cdot \mathbf{P}_b - \mathbf{r} \cdot \mathbf{H}) \cdot \hat{\mathbf{k}} + \frac{1}{\rho_0} (\mathbf{r} \cdot \mathbf{u}_{\text{top}}) \cdot \hat{\mathbf{k}} \\ & + \frac{1}{\rho_0} (\mathbf{r} \cdot \mathbf{u}_{\text{bot}}) \cdot \hat{\mathbf{k}} + \mathbf{D} \cdot \hat{\mathbf{k}} \\ & + \mathbf{r} \cdot \mathbf{h} \int_{\mathbf{H}(\mathbf{x}, \mathbf{y})}^{\mathbf{H}(\mathbf{x}, \mathbf{y}; \mathbf{t})} \zeta \mathbf{u} dz + \mathbf{r} \cdot \mathbf{h} \int_{\mathbf{H}(\mathbf{x}, \mathbf{y})}^{\mathbf{H}(\mathbf{x}, \mathbf{y}; \mathbf{t})} \frac{1}{2} \mathbf{r} \cdot \mathbf{u}_h^2 + w \frac{\partial \mathbf{u}_h}{\partial z} \cdot \hat{\mathbf{k}} \\ & + \frac{1}{\rho_0} (\mathbf{r} \cdot \mathbf{P}_a - \mathbf{r} \cdot \boldsymbol{\eta}) \cdot \hat{\mathbf{k}} + \mathbf{r} \cdot \mathbf{u}_h(z = \eta) \frac{\partial \boldsymbol{\eta}}{\partial t} \cdot \hat{\mathbf{k}}. \end{aligned} \quad (\text{A10})$$

Atmospheric pressure torque Surface undulations

Appendix B Explicit forms of the Coriolis schemes

Here we explicitly state the forms of the discrete Coriolis acceleration in the ENE, ENS, and EEN vorticity schemes for a z -coordinate system. In the ENE vorticity scheme the x and y components of the Coriolis acceleration are:

$$\begin{aligned} \text{COR}_{ij,k}^x &= \frac{1}{4e_{ij}^{1u}} f_{ij-1} v e^{1v}_{ij-1;k} + v e^{1v}_{i+1j-1;k} \\ &\quad + f_{ij} v e^{1v}_{ij;k} + v e^{1v}_{i+1j;k}, \\ \text{COR}_{ij,k}^y &= \frac{1}{4e_{ij}^{2v}} f_{i-1j} u e^{2u}_{i-1j;k} + u e^{2u}_{i-1j+1;k} \\ &\quad + f_{ij} u e^{2u}_{ij;k} + u e^{2u}_{ij+1;k}. \end{aligned} \quad (\text{B1})$$

In the ENS vorticity scheme the x and y components of the Coriolis acceleration are:

$$\begin{aligned} \text{COR}_{ij,k}^x &= \frac{1}{8e_{ij}^{1u}} v e^{1v}_{ij-1;k} + v e^{1v}_{i+1j-1;k} \\ &\quad + v e^{1v}_{ij;k} + v e^{1v}_{i+1j;k} [f_{ij-1} + f_{ij}], \\ \text{COR}_{ij,k}^y &= \frac{1}{8e_{ij}^{2v}} u e^{2u}_{i-1j-1;k} + u e^{2u}_{i-1j+1;k} \\ &\quad + u e^{2u}_{ij;k} + u e^{2u}_{ij+1;k} [f_{i-1j} + f_{ij}]. \end{aligned} \quad (\text{B2})$$

We note that each term in the ENE and ENS forms can be written in the general form of Equations 8 and 9 as $v e^{1v} = \tilde{V}/e^{3v}$ and $u e^{2u} = \tilde{U}/e^{3u}$. In the ENE and ENS cases $e_k^3(\mathbf{b}_n) = e_k^3(\mathbf{c}_n)$ in Equations 8 and 9.

In the EEN vorticity scheme, the x and y components of the Coriolis acceleration are:

$$\begin{aligned} \text{COR}_{ij,k}^x &= \frac{1}{12e_{ij}^{1u}} F_{ij,k}^{\text{NE}} v e^{3v} e^{1v}_{ij;k} + F_{i+1j,k}^{\text{NW}} v e^{3v} e^{1v}_{i+1j;k} \\ &\quad + F_{ij,k}^{\text{SE}} v e^{3v} e^{1v}_{ij-1;k} + F_{i+1j,k}^{\text{SW}} v e^{3v} e^{1v}_{i+1j-1;k}, \\ \text{COR}_{ij,k}^y &= \frac{1}{12e_{ij}^{2v}} F_{ij,k}^{\text{NE}} u e^{3u} e^{2u}_{ij;k} + F_{ij,k}^{\text{NW}} u e^{3u} e^{2u}_{i-1j;k} \\ &\quad + F_{ij+1,k}^{\text{SE}} u e^{3u} e^{2u}_{ij+1;k} + F_{ij+1,k}^{\text{SW}} u e^{3u} e^{2u}_{i-1j+1;k}, \end{aligned} \quad (\text{B3})$$

where F^{NE} , F^{NW} , F^{SE} , and F^{SW} are thickness-weighted triads of the Coriolis parameter:

$$F_{ij;k}^{\text{NE}} = \tilde{f}_{ij;k} + \tilde{f}_{i-1;j;k} + \tilde{f}_{ij;k-1}, \quad (\text{B4})$$

$$F_{ij;k}^{\text{NW}} = \tilde{f}_{ij;k} + \tilde{f}_{i-1;j;k} + \tilde{f}_{i-1;j-1;k}, \quad (\text{B5})$$

$$F_{ij;k}^{\text{SE}} = \tilde{f}_{ij;k} + \tilde{f}_{ij;k-1} + \tilde{f}_{i-1;j-1;k}, \quad (\text{B6})$$

$$F_{ij;k}^{\text{SW}} = \tilde{f}_{i-1;j;k} + \tilde{f}_{ij;k-1} + \tilde{f}_{i-1;j-1;k}, \quad (\text{B7})$$

where $\tilde{f} = f/e^{3f}$ using the EEN definition of e^{3f} shown in Equation 13.

To calculate the planetary vorticity diagnostic we take the curl of the depth-integrated Coriolis acceleration using Equations 15 and 22. In general the resulting equation of the vorticity diagnostic is very difficult to interpret. We only present the form of the planetary vorticity diagnostic for the EEN scheme on a grid with no partial cells or model level steps as it is used to derive the numerical beta effect in Section 3.5:

$$\begin{aligned} \text{PVO}_{ij} = & \frac{1}{12(e^{1f}e^{2f})_{ij}} \left(f_{ij+1}^{\text{NE}} Ve^{1v}_{ij+1} + f_{i+1;j+1}^{\text{NW}} Ve^{1v}_{i+1;j+1} \right. \\ & + f_{ij}^{\text{SE}} Ve^{1v}_{ij-1} + f_{i+1;j}^{\text{SW}} Ve^{1v}_{i+1;j-1} \\ & + f_{i+1;j+1}^{\text{SE}} Ue^{2u}_{i+1;j+1} + f_{i+1;j}^{\text{NE}} Ue^{2u}_{i+1;j} \\ & + f_{ij+1}^{\text{SW}} Ue^{2u}_{i-1;j+1} + f_{ij}^{\text{NW}} Ue^{2u}_{i-1;j} \\ & \left. + (f_{ij+1} - f_{ij-1}) Ve^{1v}_{i+1;j} + (f_{i+1;j} - f_{i-1;j}) Ue^{2u}_{ij+1} + Ue^{2u}_{ij} \right). \end{aligned} \quad (\text{B8})$$

Appendix C Alternative vorticity schemes in the double gyre model

In this section we present various integrations of the SLOPED double gyre configuration using different vorticity schemes: EEN, ENS, and ENE. All other aspects of the experiment are as described in Section 4.1. The results are shown in Figure C1. The vorticity budget is qualitatively similar between the three cases as well as the decomposition of the planetary vorticity diagnostic. It should be noted that the circulations do differ as the transports vary and the separation points of the western boundary currents change.

Appendix D Contour integration without interpolation

The interpolation of vorticity diagnostic fields and the streamfunction is discussed in Section 4.2. Linear interpolation is used to minimise the difference between the enclosed area of the true streamline and the total area of the interior F cells. In this section we present results that use uninterpolated fields from the FLAT double gyre configuration. The results are shown in Figure D1 and are qualitatively similar to the interpolated results shown in Figure 9. This example is selected to demonstrate both the qualitative similarity to interpolated results but also the reduced coherence that comes from using non-interpolated data. The non-interpolated results from the Weddell Gyre are in fact more coherent than the results shown in Figure D1.

Acknowledgments

This work was financially supported by the Natural Environment Research Council NE/S007474/1. This work used Monsoon2, a collaborative High-Performance Computing facility funded by the Met Office and the Natural Environment Research Council and used JASMIN,

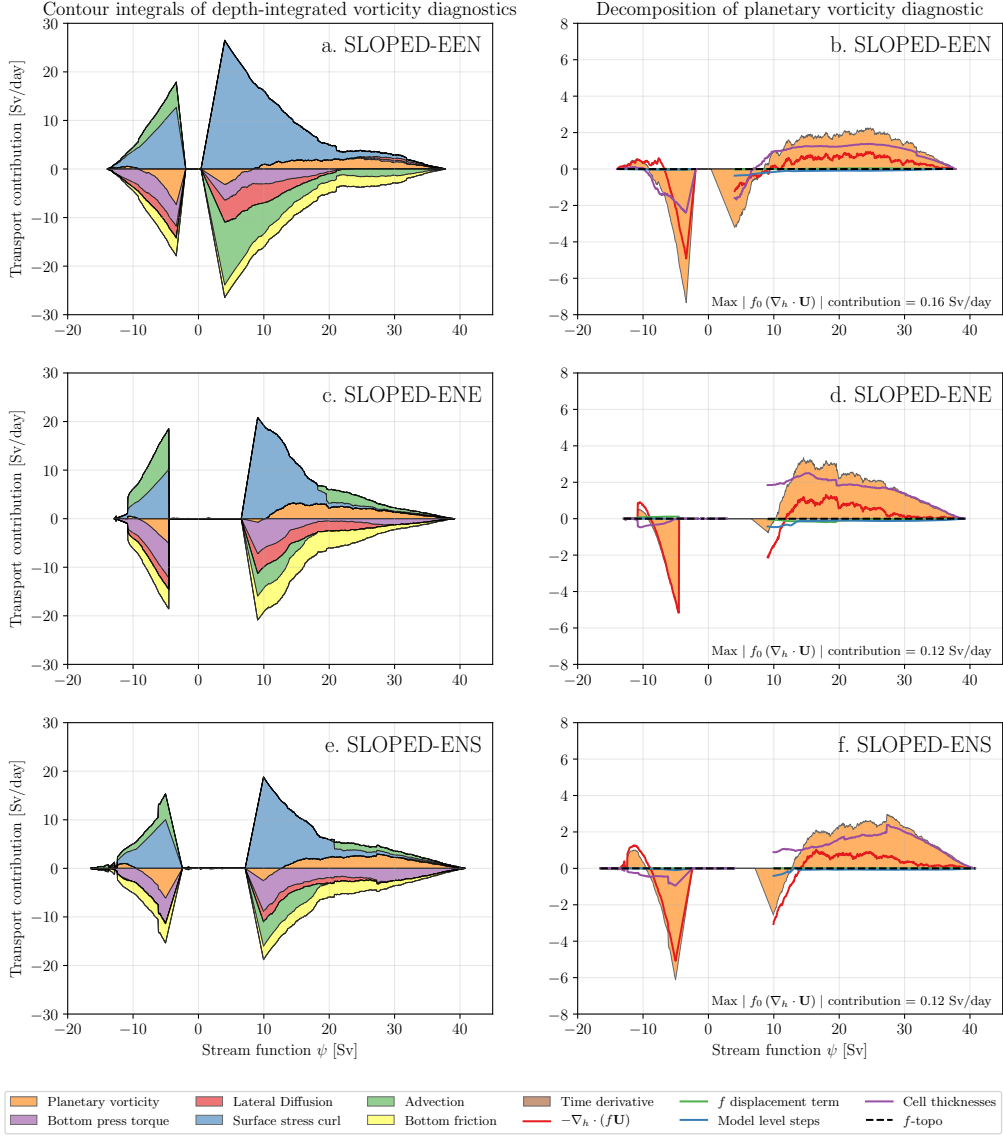


Figure C1. Stacked area plots showing the integrals of depth-integrated vorticity diagnostics for the SLOPED configuration (time-averaged) using the EEN, ENE, and ENS vorticity schemes. Positive values correspond to a force that spins the subtropical (> 0) or subpolar (< 0) gyre up. A decomposition of the planetary vorticity diagnostic integrals are given on the right (b,d,f).

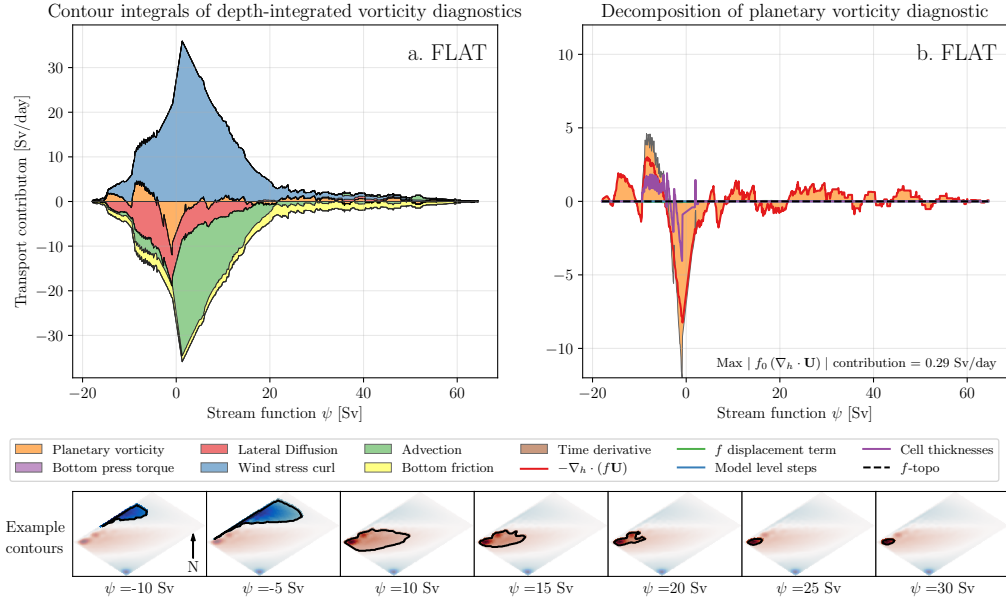


Figure D1. Stacked area plots showing the integrals of depth-integrated vorticity diagnostics (time-averaged) for the FLAT configuration without using interpolated fields. Positive values correspond to a force that spins the subtropical (> 0) or subpolar (< 0) gyre up. (b) Shows the area integrals of the planetary vorticity diagnostic and its components. The vorticity budget and decomposition are qualitatively similar to that shown in Figure 9.

the UK collaborative data analysis facility. We would like to thank Julian Mak and Andrew Coward for their assistance in configuring NEMO on Monsoon2. We would also like to thank Stephen Griffies, Hemant Khatri, and two anonymous reviewers for their detailed comments that improved the manuscript.

The software used to calculate, integrate, and plot the vorticity budget is available from <https://github.com/afstyles/VorticityContourAnalysisForNemo/tree/917f337/>. The model integrations can be found on Zenodo (Styles et al., 2022).

The global configuration used in this article uses NEMO version 4.0.4 with the following merged branches:

- branches/UKMO/NEMO_4.0.4_mirror @ 14075,
- branches/UKMO/NEMO_4.0.4_GO8_package @ 14474,
- branches/UKMO/NEMO_4.0.4_GO6_mixing @ 14099,
- branches/UKMO/NEMO_4.0.4_old_tidal_mixing @ 14096,
- branches/UKMO/NEMO_4.0.4_momentum_trends @ 15194.

The double gyre configuration uses NEMO version 4.0.1 and any modified source code is archived on Zenodo (Styles et al., 2022). The versions of NEMO and the mentioned branches can be found at <https://forge.ipsl.jussieu.fr/nemo/browser/NEMO/>.

References

- Adcroft, A., Anderson, W., Balaji, V., Blanton, C., Bushuk, M., Dufour, C. O., ... Zhang, R. (2019). The GFDL Global Ocean and Sea Ice Model OM4.0: Model

- Description and Simulation Features. *Journal of Advances in Modeling Earth Systems*, **1** (10), 3167–3211. doi: 10.1029/2019MS001726
- Amante, C., & Eakins, B. W. (2009). ETOPO1 arc-minute global relief model: procedures, data sources and analysis. *NOAA Technical Memorandum NESDIS 15*.
- Arakawa, A., & Lamb, V. R. (1981). A potential enstrophy and energy conserving scheme for the shallow water equations. *Monthly Weather Review*, **9** (1), 18–36.
- Arndt, J. E., Schenke, H. W., Jakobsson, M., Nitsche, F. O., Buys, G., Goleby, B., ... Wigley, R. (2013, jun). The International Bathymetric Chart of the Southern Ocean (IBCSO) Version 1.0-A new bathymetric compilation covering circum-Antarctic waters. *Geophysical Research Letters*, **40** (12), 3111–3117. doi: 10.1002/grl.50413
- Barnier, B., Madec, G., Penduff, T., Molines, J. M., Treguier, A. M., Le Sommer, J., ... De Cuevas, B. (2006). Impact of partial steps and momentum advection schemes in a global ocean circulation model at eddy-permitting resolution. *Ocean Modelling*, **5** (5-6), 543–567. doi: 10.1007/s10236-006-0082-1
- Bell, M. J. (1999). Vortex stretching and bottom torques in the Bryan-Cox ocean circulation model. *Journal of Geophysical Research: Oceans*. doi: 10.1029/1999jc900064
- Bleck, R. (2002, jan). An oceanic general circulation model framed in hybrid isopycnic-Cartesian coordinates. *Ocean Modelling*, **4**(1), 55–88. doi: 10.1016/S1463-5003(01)00012-9
- Cane, M. A., Kamenkovich, V. M., & Krupitsky, A. (1998). On the utility and disutility of JEBAR. *Journal of Physical Oceanography*. doi: 10.1175/1520-0485(1998)028<0519:OTUADO>2.0.CO;2
- Drijfhout, S. S., Marshall, D. P., & Dijkstra, H. A. (2013). Conceptual Models of the Wind-Driven and Thermohaline Circulation. In G. Siedler, S. M. Griffies, J. Gould, & J. A. Church (Eds.), *Ocean circulation and climate* (Vol. 103, pp. 257–282). Academic Press. doi: 10.1016/B978-0-12-391851-2.00011-8
- Gent, P. R., & McWilliams, J. C. (1990). Isopycnal Mixing in Ocean Circulation Models. *Journal of Physical Oceanography*. doi: 10.1175/1520-0485(1990)020<0150:imiocmi>2.0.co;2
- Griffies, S. M., Adcroft, A., & Hallberg, R. W. (2020). A Primer on the Vertical Lagrangian-Remap Method in Ocean Models Based on Finite Volume Generalized Vertical Coordinates. *Journal of Advances in Modeling Earth Systems*, **2** (10), 1–38. doi: 10.1029/2019MS001954
- Gula, J., Molemaker, M. J., & McWilliams, J. C. (2015). Gulf stream dynamics along the southeastern U.S. seaboard. *Journal of Physical Oceanography*, **3** (3), 690–715. doi: 10.1175/JPO-D-14-0154.1
- Hecht, M. W. (2010). Cautionary tales of persistent accumulation of numerical error: Dispersive centered advection. *Ocean Modelling*, **3** (3), 270–276. doi: 10.1016/j.ocemod.2010.07.005
- Hughes, C. W., & de Cuevas, B. A. (2001). Why western boundary currents in realistic oceans are inviscid: A link between form stress and bottom pressure torques. *Journal of Physical Oceanography*, **3** (10), 2871–2885. doi: 10.1175/1520-0485(2001)031<2871:WWBCIR>2.0.CO;2
- Jackson, L., Hughes, C. W., & Williams, R. G. (2006). Topographic control of basin and channel flows: The role of bottom pressure torques and friction. *Journal of Physical Oceanography*, **3** (9), 1786–1805. doi: 10.1175/JPO2936.1
- Jagannathan, A., Srinivasan, K., McWilliams, J. C., Molemaker, M. J., & Stewart, A. L. (2021). Boundary layer-mediated vorticity generation in currents over sloping bathymetry. *Journal of Physical Oceanography*, 1757–1778. doi: 10.1175/jpo-d-20-0253.1
- Large, W. G., & Yeager, S. G. (2009, aug). The global climatology of an interannu-

- ally varying air - Sea flux data set. *Climate Dynamics*, **3** (2-3), 341–364. doi: 10.1007/s00382-008-0441-3
- Le Bras, I. A. A., Sonnewald, M., & Toole, J. M. (2019, nov). A barotropic vorticity budget for the subtropical north atlantic based on observations. *Journal of Physical Oceanography*, **49** (11), 2781–2797. doi: 10.1175/JPO-D-19-0111.1
- Le Corre, M., Gula, J., & Tréguier, A. M. (2020). Barotropic vorticity balance of the North Atlantic subpolar gyre in an eddy-resolving model. *Ocean Science*. doi: 10.5194/os-16-451-2020
- Lemarié, F., Kurian, J., Shchepetkin, A. F., Jeroen Molemaker, M., Colas, F., & McWilliams, J. C. (2012). Are there inescapable issues prohibiting the use of terrain-following coordinates in climate models? *Ocean Modelling*, **2**, 57–79. doi: 10.1016/j.ocemod.2011.11.007
- Lévy, M., Jahn, O., Dutkiewicz, S., Follows, M. J., & D’Ovidio, F. (2015). The dynamical landscape of marine phytoplankton diversity. *Journal of the Royal Society Interface*. doi: 10.1098/rsif.2015.0481
- Lévy, M., Klein, P., Tréguier, A. M., Iovino, D., Madec, G., Masson, S., & Takahashi, K. (2010). Modifications of gyre circulation by sub-mesoscale physics. *Ocean Modelling*, **3** (1-2), 1–15. doi: 10.1016/j.ocemod.2010.04.001
- Madec, G., Bourdallé-Badie, R., Chanut, J., Samson, E. C., Coward, A., Ethé, C., ... Samson, G. (2019, oct). *NEMO ocean engine*. Zenodo. doi: 10.5281/zenodo.1464816
- McDougall, T. J., & Barker, P. M. (2011). Getting started with TEOS-10 and the Gibbs Seawater (GSW) oceanographic toolbox. *SOFSO WG*, **2**, 1–28. Retrieved from <https://www.teos-10.org/>
- Mesinger, F., & Arakawa, A. (1976). Numerical methods used in atmospheric models. *NCAR Publication Series*, **7**, 1–161
- Niiler, P. P. (1966, aug). On the theory of wind-driven ocean circulation. *Deep Sea Research and Oceanographic Abstracts*, **3** (4), 597–606. doi: 10.1016/0011-7471(66)90591-2
- Perezogin, P. (2019). Deterministic and stochastic parameterizations of kinetic energy backscatter in the NEMO ocean model in Double-Gyre configuration. In *Conference on Earth and Environmental Science*. doi: 10.1088/1755-1315/386/1/012025
- Ruggiero, G. A., Ourmières, Y., Cosme, E., Blum, J., Auroux, D., & Verron, J. (2015). Data assimilation experiments using diffusive back-and-forth nudging for the NEMO ocean model. *Nonlinear Processes in Physics*. doi: 10.5194/npg-22-233-2015
- Sadourny, R. (1975). The Dynamics of Finite-Difference Models of the Shallow-Water Equations. *Journal of Physical Sciences*, **2** (4), 680–689. doi: 10.1175/1520-0469(1975)032<0680:TDOFDMi>2.0.CO;2
- Schoonover, J., Dewar, W., Wienders, N., Gula, J., McWilliams, J. C., Molemaker, M. J., ... Yeager, S. (2016). North Atlantic barotropic vorticity balances in numerical models. *Journal of Physical Oceanography*. doi: 10.1175/JPO-D-15-0133.1
- Song, Y., & Haidvogel, D. (1994). A Semi-implicit Ocean Circulation Model Using a Generalized Topography-Following Coordinate System. *Journal of Physical Oceanography*, **5** (1), 228–244. doi: 10.1006/jcph.1994.1189
- Stewart, A. L., McWilliams, J. C., & Solodoch, A. (2021). On the Role of Bottom Pressure Torques in Wind-Driven Gyres. *Journal of Physical Oceanography*, **5** (5), 1441–1464. doi: 10.1175/jpo-d-20-0147.1
- Stommel, H. (1948). The westward intensification of wind-driven ocean currents. *Transactions of the American Geophysical Union*. doi: 10.1029/TR029i002p00202
- Storkey, D., Blaker, A. T., Mathiot, P., Megann, A., Aksenov, Y., Blockley, E. W.,

- ... Sinha, B. (2018, aug). UK Global Ocean GO6 and GO7: A traceable hierarchy of model resolutions. *Geoscientific Model Development*, **1** (8), 3187–3213. doi: 10.5194/gmd-11-3187-2018
- Styles, A. F., Bell, M. J., Marshall, D. P., & Storkey, D. (2022). *De for Sea forecasting the world budget oceanographic grid*. Zenodo. doi: 10.5281/zenodo.5513825
- Vallis, G. K. (2017). Atmospheric and oceanic fluid dynamics: Fundamentals and large-scale circulation, second edition. *Physical and Oceanic Fluid Dynamics: Fundamentals and Large-Scale Circulation*, 1–946. doi: 10.1017/9781107588417
- Van Der Walt, S., Schönberger, J. L., Nunez-Iglesias, J., Boulogne, F., Warner, J. D., Yager, N., ... Yu, T. (2014, jun). Scikit-image: Image processing in python. *PeerJ*, **2** (1), e453. doi: 10.7717/peerj.453
- Willebrand, J., Barnier, B., Böning, C., Dieterich, C., Killworth, P. D., Le Provost, C., ... New, A. L. (2001, jan). Circulation characteristics in three eddy-permitting models of the North Atlantic. *Progress in Oceanography*, **3** (2-3), 123–161. doi: 10.1016/S0079-6611(01)00003-9
- Yeager, S. (2015). Topographic coupling of the atlantic overturning and gyre circulations. *Journal of Physical Oceanography*. doi: 10.1175/JPO-D-14-0100.1